Particle Formation in Laminar Flames Inhibited by Metals

Gregory T. Linteris
National Institute of Standards and Technology
and
Marc D. Rumminger
Cleaire Advanced Emission Controls

Abstract

Some organometallic compounds of iron are two orders of magnitude more effective at low volume fraction than CF_3Br in premixed flames, an order of magnitude more effective in counterflow diffusion flames, but nearly ineffective in co-flow diffusion flames. The condensation of active gas-phase iron-containing intermediates to particles is believed to be the cause of the loss of effectiveness. The present paper reviews previous work on gas-phase inhibition by iron compounds as well as the role of particles in $Fe(CO)_5$ inhibition of those flames. The understanding obtained from those simpler configurations is used to interpret new measurements of flame inhibition and particle formation in cup-burner flames of methane and air with iron, tin, manganese and bromine compounds added to the air stream.

Introduction

Production of the effective and widely used brominated fire suppressant CF_3Br (Halon 1301) and similar compounds has been halted because of their deleterious effects on stratospheric ozone [1]. While short term replacements have been suggested [2-4], they are much less effective than CF_3Br, and a better agent is desired. Recent attention has focused on phosphorus [5-8] and metal species [9-11]. The reasons these agents have attracted interest is because they are many times more effective than CF_3Br at reducing the flame speed of hydrocarbon flames when added at low volume fraction. For example, Figure 1 shows the comparative ability of CO_2 and CF_3Br, and compounds of tin, phosphorus, manganese, and iron at reducing the burning velocity of premixed flames. CF_3Br is shown to be about seven times more effective than CO_2 at reducing the flame speed, and the super-effective agents are shown, for low volume fractions, to be one to two orders more effective than CF_3Br.

If some means could be developed to use non-toxic forms of the active element, very effective fire suppressants may be possible. For example, metal species could be effective additives to fire suppressant blends for uninhabited spaces [12]. Nonetheless, recent work has shown that while the metal compounds are very effective in both premixed and counterflow diffusion flames at
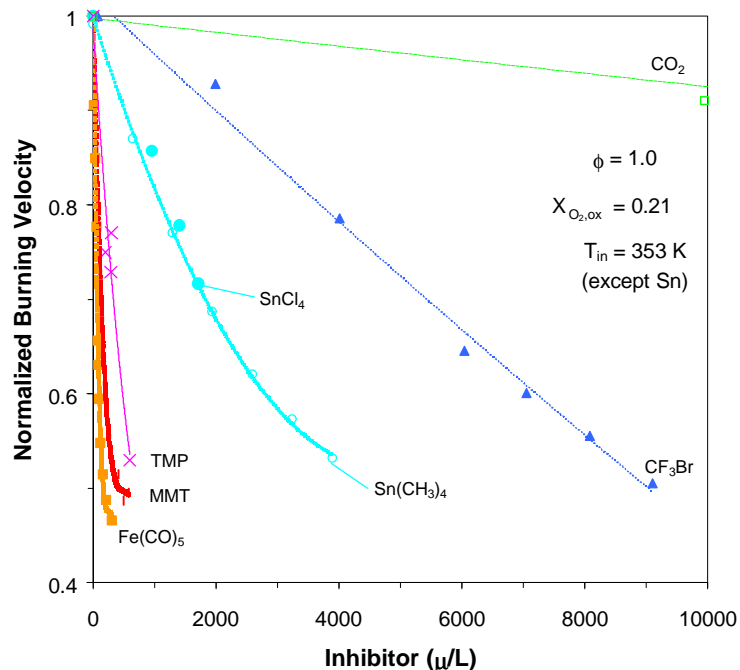
Figure 1 - Normalized burning velocity of premixed $CH_4/O_2/N_2$ flames inhibited by CO_2, CF_3Br, $Sn(CH_3)_4$, $SnCl_4$ [13], MMT, TMP [14], and $Fe(CO)_5$ (T_{in} = 353 K for all data except $Sn(CH_3)_4$ and $SnCl_4$ which are at 298 K). Lines are curve fits to data.

low volume fraction, their marginal effectiveness decreases rapidly above a volume fraction of a few hundred $\mu L/L$[1]. Further, their effectiveness in flames resembling fires (e.g., cup-burner type co-flow diffusion flames) was found to be much less than expected based on the results in the premixed and counterflow diffusion flames [15].

The goal of the present work is to investigate the flame parameters that lead to the loss of effectiveness of these otherwise powerful inhibitors. Background information on the flame inhibition mechanism of metals is presented. Previously obtained results from particle measurements in premixed and counterflow diffusion flames are described, as are calculations which estimate the maximum effect from heterogeneous versus homogeneous radical scavenging mechanisms. We also present new data on the effectiveness of metals in co-flow diffusion flames of the cup burner configuration, and present the results of laser scattering measurements of particles in cup-burner flames inhibited by $Fe(CO)_5$. Particle formation within the high-temperature region of the flame is shown to be an important loss mechanism for the active inhibiting species. Further, particle movement (by convection or thermophoresis) is shown to provide an even stronger loss mechanism for the active species by preventing them from reaching the regions of high chain-carrying radical volume fraction where they are needed to provide chemical inhibition.

---

[1] Note that $\mu L/L$ is equivalent to ppm by volume.

Background

It has been known for some time that metals at ppm levels recombine radicals in the post-combustion region of premixed flames [16] more bulewicz, and early work demonstrated the flame inhibition potential of $Pb(C_2H_5)_4$, CrO_2Cl_2, and $Fe(CO)_5$ in hydrocarbon/N_2/O_2 premixed flames [13,17,18]. Recently, the agents tetramethyltin ($Sn(CH_3)_4$, TMT), methylcyclopentadienylmanganese tricarbonyl ($CH_3C_5H_4Mn(CO)_3$, MMT), ferrocene ($Fe(C_5H_5)_2$) and iron pentacarbonyl ($Fe(CO)_5$) have been studied in some detail [10,11]. Experiments and modeling of $Fe(CO)_5$ have quantified its performance and explained its mechanism of inhibition for a variety of conditions [19-21]. For iron, the strong inhibition is believed to occur from a catalytic radical recombination cycle involving iron oxides and hydroxides:

$$FeOH + H \leftrightarrow FeO + H_2$$
$$FeO + H_2O \leftrightarrow Fe(OH)_2$$
$$Fe(OH)_2 + H \leftrightarrow FeOH + H_2O$$

$$\text{net reaction: } H + H \leftrightarrow H_2.$$
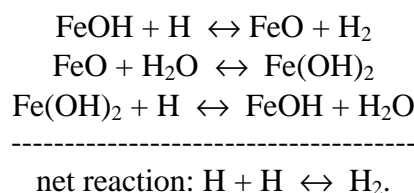
For manganese-containing inhibitors, the mechanism is believed to be similar (with Mn replacing Fe in the reaction sequence). For tin, the inhibition reactions are thought to be:

$$SnO + H + M \leftrightarrow SnOH + M$$
$$SnOH + H \leftrightarrow SnO + H_2$$

$$\text{net: } H + H \leftrightarrow H_2$$
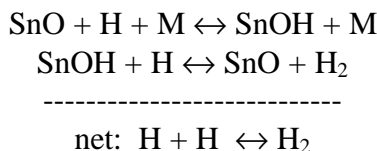
At low volume fractions, $Fe(CO)_5$ is about eighty times more effective than CF_3Br at reducing the burning velocity of premixed flames, MMT forty times, and TMT three times. Kinetic modeling of the flame inhibition has lead to an understanding of the reasons why these metallic agents differ in their effectiveness. Both manganese monoxide and iron monoxide can react with H_2O to form the stable di-hydroxide intermediate (e.g., $Fe(OH)_2$ and $Mn(OH)_2$), which can then react with H atom directly. Conversely, the di-hydroxide of tin has not been observed for the present conditions. The intermediate species SnO relies upon a three-body reaction with H atom to form the hydroxide, and the reaction is rate-limiting and slow. Further, iron is superior to manganese in premixed flames because the equilibrium for the reaction $FeO + H_2O \leftrightarrow Fe(OH)_2$, unlike the equivalent relation for manganese species, favors the di-hydroxide, so it can exist in high concentrations to react with H atoms.

For premixed flames, all of these organometallic agents lose their effectiveness at a relatively low volume fractions. For $Fe(CO)_5$, there is a very large change in its effectiveness at about 100 $\mu L/L$. This is believed to occur from condensation of the active iron-containing intermediates to particles [22]. In a similar fashion, MMT loses its effectiveness at about 300 $\mu L/L$, and TMT loses its marginal effectiveness at about 3000 $\mu L/L$. Indeed, if added directly to a cup-burner flame alone, $Fe(CO)_5$ is not expected to be a particularly effective suppressant because condensation of active iron-containing intermediates to particles limits their gas-phase volume

3

fraction, restricting the potential of the gas-phase catalytic cycle. Any practical fire suppressant using these super-effective agents would require some method to overcome the loss of effectiveness.

The primary motivation of the present work is to describe the effect of particle formation on flame inhibition. Laser-light scattering experiments are used to determine the particle formation region and to estimate the particle size. Thermophoretic sampling with transmission electron microscopy provide the particle size and morphology. The premixed flame experiments use Bunsen-type flames of CH_4-O_2-N_2 and CO-H_2-O_2-N_2. By making proper choices of concentrations and gas flows, the effects of both flame temperatures and residence time on particle formation are studied. The unresolved issue of whether the inhibition is heterogeneous or homogeneous is addressed, and results are presented for inhibition by an ideal heterogeneous inhibitor. We also present data on particle formation in counterflow diffusion flames of methane and air (with agent addition to either the fuel or air stream), and cup-burner type co-flow diffusion flames of methane and air with TMT, MMT, and $Fe(CO)_5$ added to the air stream together with CO_2. The longer residence time diffusion flame burners demonstrate the roles of particle formation and flow field effects in the loss of active species from the gas-phase inhibiting region of the flame.

Experiment

Three flame types were tested with the organometallic inhibitors: premixed, counterflow diffusion, and co-flow diffusion flames. The burners used to produce these flames are described below, along with the common gas-handling system and the optical system used for particle detection. The thermophoretic sampling system for collection of the nanoparticles (subsequently analyzed by transmission electron microscopy) is also described. These are followed by discussion of measurement uncertainty.

Burners

The premixed burner system, described previously [9,21,23], has been used for flame speed measurements using the total area method [24]. Premixed flames (ϕ=1.0) were stabilized on a Mache-Hebra nozzle burner (inner diameter 1.02 cm $\pm$ 0.005 cm) [25] with an air co-flow. The burner produces a steady, straight-sided, conical, non-sooting flame with a height of 13 mm. The burner and annulus for the co-flowing air were housed in an acrylic chimney with three optical access holes. Rubber bellows connect the chimney with the adjacent optical elements to provide a flexible and airtight seal. The premixed flame conditions correspond to those of the $Fe(CO)_5$ inhibition measurements described in Refs. [9] and [21].

The counterflow burner system has been described previously [9,26]. The fuel and oxidizer tubes (22.2 mm diameter) are separated by 11 mm, and there is a nitrogen shroud flow from a concentric annulus (51 mm diameter) around the bottom (oxidizer) jet. The burner produces a non-sooting flame with a flat region in the center. The strain rate a (the derivative of the velocity with respect to the axial position) is approximated from the outer flow jet exit velocities as $a = \left(2|V_O|/L\right)\left(1 + |V_F|\sqrt{\rho_F}/|V_O|\sqrt{\rho_O}\right)$, where L is the jet separation distance, V_i is the velocity of gas i (F=fuel, O=oxidizer), and ρ_i is the density of gas i [27]. The jet exit velocities were chosen

4

so that the momentum of the two streams were balanced at all values of the strain rate; that is, $\rho_F V_F^2 = \rho_O V_O^2$.

The cup burner, described previously [28,29], consists of a cylindrical glass cup (28 mm diameter) positioned inside a glass chimney (53.3 cm tall, 9.5 cm inner diameter). To provide uniform flow, 6 mm glass beads fill the base of the chimney, and 3 mm glass beads (with two 15.8 mesh/cm screens on top) fill the fuel cup. The traditional cup-burner was modified slightly for optical access. To prevent laser light from scattering off of the cup-burner chimney walls, the round cup-burner chimney was cut off to a height 2 mm below the fuel cup rim and a second, square chimney (as in the premixed flame experiments described above), with an additional co-flow of air, enclosed the round chimney and burner.

The organometallic inhibitors were added to the flames using multi-stage saturators in controlled temperature baths. The $Fe(CO)_5$ and TMT used two-stage saturators of a design described previously [21], while the MMT used a three-stage saturator, with 50 % larger stages, to insure saturation. A measured portion of the added carrier gas (N_2, CO_2, or CH_4) flowed in series through the saturators, and was then added to the bulk flow of that gas. The volume fraction of the organometallic inhibitors in the air stream was calculated based on the measured bulk flow, measured carrier gas flow, and calculated vapor pressure of the agent at the bath temperature. The experimental vapor pressure data was obtained from refs. [30-32]. Tests to validate the assumption of agent saturation in the carrier gas have been described previously [21].

Gas flows were measured with digital mass flow controllers (Sierra Model 860[2]) with a claimed repeatability of 0.2 % and accuracy of 1 % of full-scale flow, which have been calibrated with piston, bubble, and dry flow meters so that their accuracy is 1 % to 2 % of the indicated flow. The fuel gases were methane (Matheson UHP), carbon monoxide (Matheson UHP) and hydrogen (Matheson UHP). The oxidizer consisted of nitrogen (boil-off from liquid N_2) and oxygen (MG Industries), or air, from house compressed air (filtered and dried) which was additionally cleaned by passing it through an 0.01 µm filter, a carbon filter, and a desiccant bed to remove small aerosols, organic vapors, and water vapor. All experiments were performed at ambient pressure. The chemicals used were $Fe(CO)_5$ (Aldrich), TMT (Alfa Aesar), MMT (Alfa Aesar), and CO_2 (Airgas).

Optical System

Light-scattering and extinction techniques with phase-sensitive detection were used to determine particle location and properties. The apparatus, shown in Figure 2, is similar to those used by other researchers [33,34]. The light source is a 4-W argon-ion laser (Spectra Physics BeamLok 2060), with a vertically-polarized 2.2-W beam at 488 nm. A mechanical chopper (Stanford Research 640) modulates the beam at 1500 Hz and provides a reference signal for the lock-in amplifiers. A polarization-preserving single-mode optical fiber (3 µm diameter) carries the light into a chemical fume hood (90 cm x 150 cm x 150 cm) which contains the burner. At the fiber

---

[2] Certain commercial equipment, instruments, or materials are identified in this paper to adequately specify the procedure. Such identification does not imply recommendation or endorsement by the National Institute of Standards and Technology, nor does it imply that the materials or equipment are necessarily the best available for the intended use.

output, collimating optics, a polarization rotator, mirrors and a focusing lens (f = 250 mm) deliver the laser light to the test region. A glass wedge between the polarization rotator and the focusing lens diverts a small fraction of the beam to a reference detector which monitors the laser power during the experiments. The transmission efficiency for the laser-to-fiber coupling system is only about 15 %, but this provides sufficient power for the experiments. The steep temperature gradients in the present flames cause significant beam steering and distortion. These effects, if unmitigated, would produce fluctuations of a few percent in the measured transmissivity, which is approximately the same magnitude as the peak absorptivity ($<$ 2 %). To reduce the beam steering effect in the premixed and counterflow diffusion flame burners, we follow an approach used by Dibble [35] and Nguyen [36], which involves reflecting the beam back through the flame along the same path, thus "unsteering" it. The approach has the

focus. A concave spherical mirror (f
and a glass wedge sends it to an integrating sphere. To spatially probe the flames, a three-axis translation stage (minimum step size of 0.0016 mm) positions the burner and chimney in the
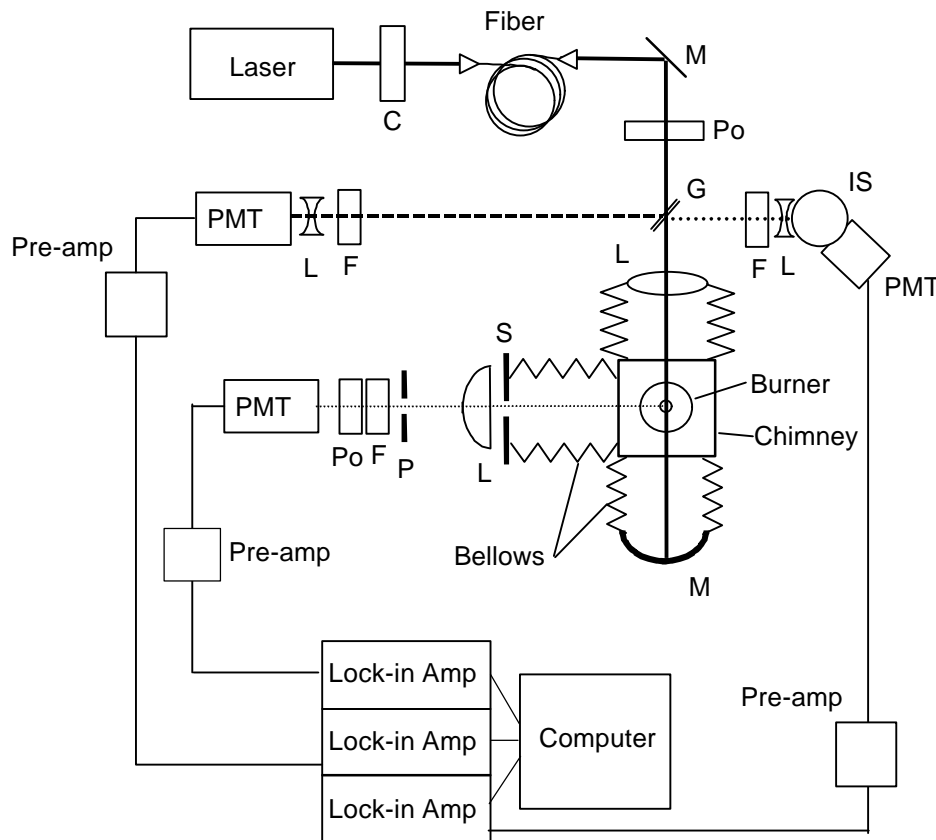
Figure 2: Schematic of laser scattering/extinction system: C, chopper; M, mirror; G, beam pick-off; L, lens; S, spatial filter (circular aperture); Po, polarizer; F, laser-line and neutral density filters; PMT, photomultiplier; P, pinhole; IS, integrating sphere (from ref.: [22]).

The light detection system consists of three photomultiplier tubes (PMT, all type 1P28) with appropriate filtering. The reference PMT has neutral density filters and a laser-line filter ($\Delta\lambda$ = 10 nm $\pm$ 2 nm). The detection system for light scattered normal to the laser beam consists of a circular aperture (5 mm diameter), collection lens (f = 100 mm), pinhole aperture (diameter 1 mm), laser-line filter, polarizer and PMT. For the 90°-scattered light, the circular aperture (5 mm diameter) located 10 cm from the laser beam focus provides a solid angle of 0.002 sr. The pinhole aperture (1 mm diameter) defines the length of the sample to be 1 mm based on unity magnification.

The signal from each of the detectors is pre-amplified (Stanford Research 552) before entering a lock-in amplifier (Stanford Research 530). A personal computer controls the amplifiers and records the measurements during the experiments using a data acquisition card (Strawberry Tree DynaRes Ultra 8). In the data acquisition software, each scattering or transmission data point is normalized by the reference signal. Typically, 100 readings are averaged over a time of about 1 second; post-processing software reduces the data and calculates uncertainty as described below. The measured quantities in the experiment are the voltage outputs of the reference, transmission, and scattered light detectors, and these depend on the system geometry, optical efficiencies, detector responsivity, gas density and particle number density, and the scattering cross section of the gases or particles. To obtain the scattering cross section (Q_{vv}) of the gases or particles in the flame, a calibration of the optical system efficiency is performed using a gas with known scattering cross section [37,38] (ethylene is used because of its relatively large cross section). The scattering and transmission signals are measured for the calibration gas to give a calibration factor, $C = Q_{vv,cal}\dfrac{t_{cal}}{S_{vv,cal}}$, where $Q_{vv,cal}$ is the known scattering cross section of the calibration gas, t_{cal} is the transmissivity of the calibration gas, and $S_{vv,cal}$ is the scattering signal caused by the calibration gas. Given the calibration constant and scattering measurements, the scattering cross section at each location can be found as $Q_{vv} = C\dfrac{S_{vv}}{t_I}$, where S_{vv} is the measured scattering signal and τ_I is the transmissivity of the flame gases and particles.

Thermophoretic Sampling

Thermophoretic sampling with transmission electron microscopy (TEM) is used as a supplemental technique to determine particle size and morphology. The procedure and apparatus are similar to those used by Dobbins and Megaridis [39] and Koylu et al. [40]. A computer-controlled, double-acting piston with travel of 5.08 cm quickly inserts and removes the electron microscope grid from the flame. Transit times and the dwell time in the flame were measured using a laser, mirror, photodiode, and oscilloscope [40]. Each grid is attached to a stainless steel substrate with thickness of 0.4 mm, and height between 3 mm to 5.7 mm. The EM grids are copper with a carbon film deposited on one side (Electron Microscopy Sciences p/n CFH4-SPEC-CU), and are fastened onto the metal substrates using adhesive or double-sided tape.

Uncertainty Analysis

The uncertainty analysis consists of calculation of individual uncertainty components and their root mean square sums [41]. All uncertainties are reported as *expanded uncertainties*: $X \pm U$, where U is ku_c, and is determined from a combined standard uncertainty (estimated standard deviation) u_c, and a coverage factor $k = 2$ (level of confidence approximately 95 %). Likewise, when reported, the relative uncertainty is $U / X \cdot 100$ %, or $ku_c / X \cdot 100$ %.

The expanded relative uncertainties for the experimentally determined quantities in this study are as follows: 6.5 % to 11.5 % for $Fe(CO)_5$ volume fraction, 1.4 % for equivalence ratio, 1.1 % for oxygen volume fraction, 1.2 % for hydrogen volume fraction in the reactants, and between 1 % and 5 % for normalized burning velocity and 1 % to 5 % for the normalized extinction strain rate (the *normalized* burning velocity is defined as the burning velocity of the inhibited flame divided by the burning velocity of the uninhibited flame, and likewise for the extinction strain rate). For the scattering measurements, the combination of slight fluctuations in the flame position, small particle scattering cross section, steep spatial gradients in the flame, and system noise cause the scattering signal to vary about a local mean value at any given location. The expanded relative uncertainty of the Q_{vv} for the premixed and counterflow diffusion flames is no more than 10% of the mean in the particle zone and no more than 20% of the mean in the unburned reactants. The expanded relative uncertainty in the extinction volume fraction for CO_2 added to the cup burner is 4 %, and for the added organometallic agents, CF_3Br, and Br_2 , 5 %, 2.7 %, and 2 %, respectively.

Results and Discussion

Premixed Flames(ϕ=1.0)

The premixed methane-air Bunsen-type flame with $Fe(CO)_5$ added to the reactant stream showed a scattering signal which varied greatly with the position in the flame [22]. Figure 3 hows the scattering signal as a function of distance from the burner centerline along a horizontal profile 7 mm above the burner base. At this measurement height, the Bunsen cone has a radius of about 2.3 mm (the diameter of the burner exit nozzle is shown at the base of the figure). As the figure shows, there are two scattering peaks within the flame region (one for each side of the Bunsen cone). Far outside the flame region (i.e., downstream of the flame in the product gases), the scattering signal is two orders of magnitude larger than the in-flame signal, indicating very large or numerous particles. These downstream particles have little consequence for the flame inhibition by iron species; instead, it is the in-flame particles which affect the performance of $Fe(CO)_5$ in this flame, and we concentrate our discussion on the in-flame particles.

8
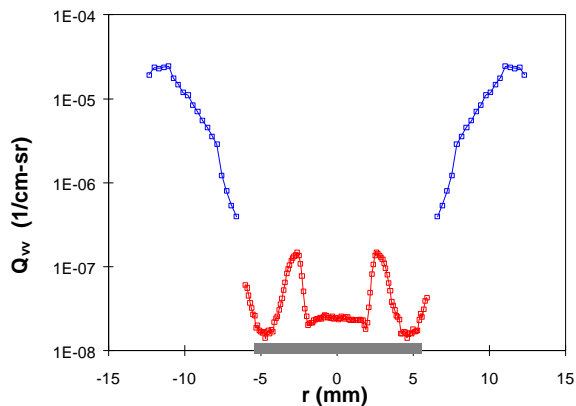
Figure 3: Scattering cross section Q_{vv} as a function of the radical distance r from the burner centerline at 7 mm height in stoichiometric CH₄-air flame with 200 µL/L of Fe(CO)₅ (from ref.: [22]).
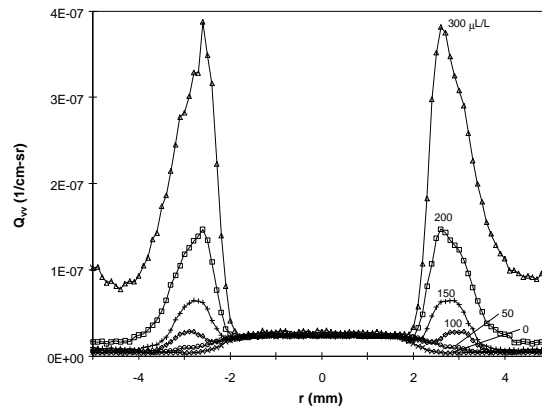
Figure 4: Measured scattering cross section through a stoichiometric CH₄-air flame 7 mm above the burner rim at various inhibitor volume fractions (from ref.: [22]).

The in-flame particles are present near the region of peak reaction rate of H-atom, which is also near the region where the inhibiting species (FeO, FeOH, and Fe(OH)₂) are most active [42]. Hence, the particles can act as sinks for the inhibiting iron-containing intermediate species. As the particles are carried further into the flame, the temperature rises, and they disappear. Only very far downstream (r>6 mm) do the particles reappear, but this location is too far removed from the radical chain-branching region to have much effect on the burning velocity. For those large values of *r*, the velocity is decreasing, leading to a larger residence time, and the temperature is decreasing (due to heat losses and co-flow air entrainment); both of these effects can lead to the very large scattering signal at that location. Figure 4 shows the in-flame particle region in more detail. Scattering data are shown for Fe(CO)₅ volume fractions in the reactant stream of (0, 50, 100, 150, 200, and 300) µL/L. The curve for 0 µL/L of inhibitor (the bottom curve in the figure) clearly shows the difference in scattering by the reactant and products species (which have a different density and composition). The scattering signal increases with increasing amounts of Fe(CO)₅.

Since the loss of effectiveness in premixed flames inhibited by Fe(CO)₅ was postulated to be caused by condensation of iron-containing intermediate species to particles, it is of interest to compare how the loss of effectiveness correlates with the particle scattering signal. The presence of particles is characterized by the height of the scattering peak above the background scattering caused by the gas-phase species at the same physical location in the flame (approximately the height of the peaks in Figure 4). Figure 5 shows data for the normalized burning velocity (left axis), and the maximum value of the in-flame scattering (right axis), as a function of the volume fraction of added Fe(CO)₅. To provide variation in the manner in which the inhibitor loses its effectiveness, curves are provided for two values of the oxygen volume fraction in the oxidizer $X_{O_2,ox}$, 0.21 and 0.244. Referring to the two curves for $X_{O_2,ox} = 0.21$ in Figure 5, the value of the volume fraction of added inhibitor X_{inh} at which the great loss of effectiveness occurs (i.e., the slope changes dramatically) is about 100 µL/L, and this volume fraction also corresponds to the

point at which the scattering signal starts to rapidly increase in magnitude. The curves for $X_{O_2,ox}$ = 0.244 indicate that loss of effectiveness of $Fe(CO)_5$ occurs at a higher value of X_{inh} than for $X_{O_2,ox}$ =0.21, and that the increase in particle scattering is also retarded until a larger quantity of $Fe(CO)_5$ is added. The curves in Figure 5 indicate that the formation of particles is correlated with a *loss* of effectiveness of $Fe(CO)_5$, rather than being associated with the strong inhibition itself.
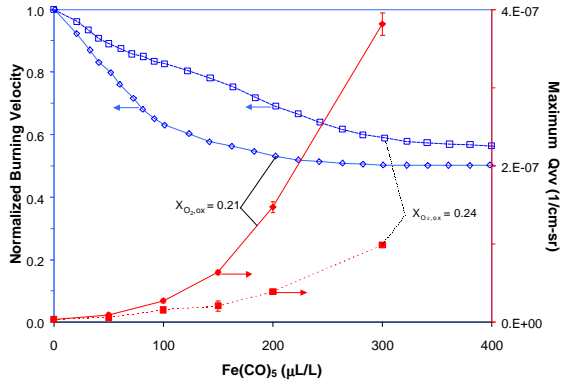
Figure 5: Normalized burning velocity (from Ref. [9]) and maximum Q_{vv} for ϕ=1.0 CH$_4$ flame with $X_{O_2,ox}$ = 0.21 and 0.24 (from ref.: [22]).
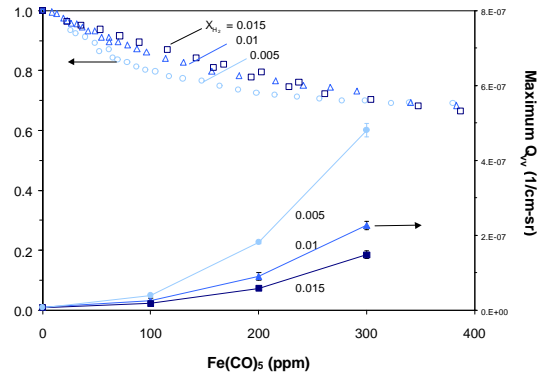
Figure 6: Maximum scattering signal and normalized burning velocity (from ref. [21]) for CO-H$_2$ flames as $Fe(CO)_5$ concentration varies (from ref.: [22]).

Two features of the higher oxygen volume fraction flames may be causing the loss of effectiveness to occur at a higher value of X_{inh}. The larger value of $X_{O_2,ox}$ leads to a higher final temperature of the flame, which would hinder condensation, requiring a larger value of X_{inh} for an equivalent amount of scattering. Alternatively, the higher temperature flames have a higher flame speed, which provides a shorter residence time in the flame for particle inception and growth. In order to examine which of these effects is important for particle formation and loss of effectiveness of $Fe(CO)_5$, experiments with varying $X_{O_2,ox}$ and fuel type were conducted.

In order to obtain flames with nearly identical adiabatic flame temperatures but varying residence times (i.e., flame speeds) we conducted experiments with $CO/O_2/N_2/H_2$ mixtures, with varying hydrogen volume fraction. The normalized burning velocity and peak in-flame scattering signal for flames with H$_2$ volume fractions X_{H_2} of 0.005, 0.010, and 0.015 are shown in Figure 6. As the figure shows, the flames with less H$_2$ (slower flames, longer residence times) lose their effectiveness at lower values of X_{inh}, and these flames also have particle scattering signals which rise faster at lower values of X_{inh}.

The data for a collection of experiments having a range of burning velocity and peak adiabatic flame temperature show the importance of residence time for particle formation. Figure 7 shows the peak in-flame scattering signal for methane and CO flames with varying peak temperature, burning velocity, and $Fe(CO)_5$ loading. Each solid line is a linear least-squared fit to all of the

10

data at a certain value of X_{inh}, namely (100, 200, and 300) μL/L of Fe(CO)$_5$., which are noted by circles, diamonds, and squares, respectively. Within each data set for an inhibitor loading, the points correspond to: (h)igh, (m)edium, and (l)ow temperature, and CH$_4$ flames (open symbols) and CO flames (closed symbols). As Figure 7 shows, the scattering signal is clearly related to the burning velocity, which is inversely related to the residence time. Similar plots investigating the importance of peak flame temperature did not show its correlation with the scattering signal.
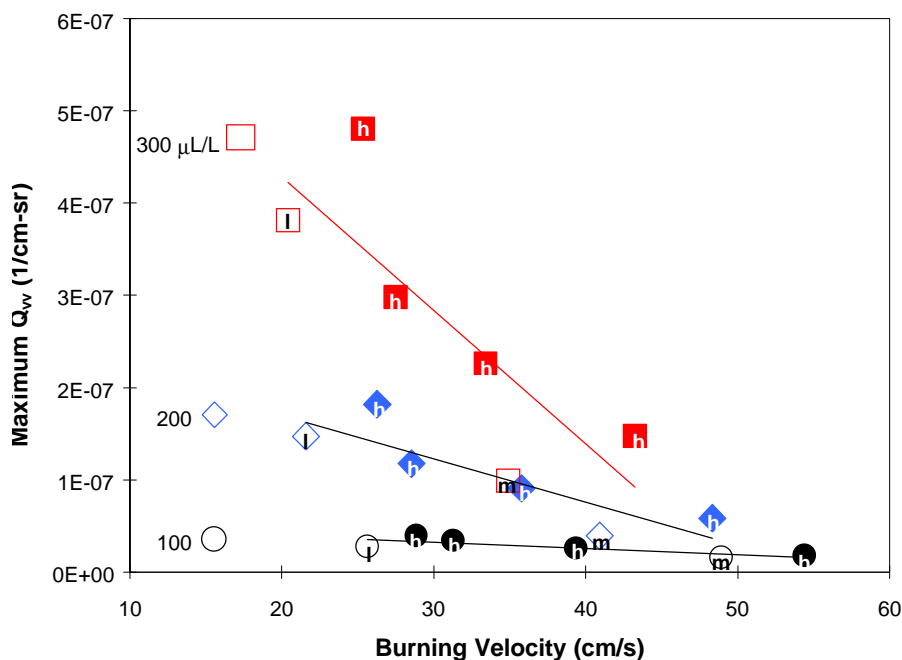
Figure 7: Maximum Q_{vv} for flames of CH$_4$ (open symbols) and CO (closed symbols) as a function of the burning velocity. The letters correspond to the adiabatic flame temperature (low, medium, and high, 2220, 2350, and 2470 K), while the symbol shape (square, diamond, and circle) corresponds to the loading of Fe(CO)$_5$: (100, 200 , and 300) μL/L (from ref. [22]).

Particle Size and Morphology in Premixed Flames

Further insight into the particle properties can be extracted from the scattering signals (e.g., Figure 4) by using other information available [22]. For example, we may assume that 50 % to 100 % of the iron in the feed stream condenses to particles. Previous calculations using a gas-phase only mechanism for the flame inhibition by Fe(CO)$_5$ were in good agreement for low volume fraction, but deviated once the inhibitor reached the volume fraction at which it lost its marginal effectiveness [19]. The amount of deviation corresponds to condensation of about 50 % of the available Fe(CO)$_5$ (X_{inh}=200 μL/L), and an upper limit of particle mass is obtained assuming 100 % condensation. Other reasonable assumptions (for estimation purposes) are that the particles are monodisperse Rayleigh scatterers composed of FeO. Using the scattering signals collected for 200 μL/L of added Fe(CO)$_5$, we estimate that for 50 % and 100 % condensation, the particles have, respectively, a volume fraction of 1.2×10^{-8} and 2.2×10^{-8}, diameter of 16 nm and 13 nm, and number density of 5.3×10^9 cm^{-3} and 2.1×10^{10} cm^{-3}. Using the

optical and bulk properties of Fe instead of FeO increases the inferred diameter by 15 % and the number density by 9 %.

For the counterflow diffusion flames, both laser scattering and laser extinction measurements were possible for some conditions. It was found [43], that for low strain rate flames, the particles have diameters between 10 nm and 30 nm, number densities of 10^8 cm^{-3} to 10^{10} cm^{-3}, and volume fractions of 10^{-7} to 10^{-8}. The mean diameter and volume fraction of the particles generally increased with increasing Fe(CO)$_5$ loading.

Additional information on the particle properties is obtained from thermophoretic sampling of the flames. For the premixed flames, the 3 mm diameter TEM grid was inserted at a height of 7 mm above the burner rim, and at a location corresponding to the main reaction zone of the flame (r = (2.7 ± 0.3) mm). The image shown in Figure 8 corresponds to a dwell time of 375 ms in a flame with X_{in} = 200 µL/L. The particles show a moderate degree of agglomeration, with about 1 to 10 primary particles per agglomerate and primary particle sizes of under 20 nm. The primary particle diameters from the TEM images are in reasonable agreement with those estimated above from the scattering signal (assuming 50 % to 100 % of the iron species condense). These small diameters, 10 nm to 20 nm, support the possibility of particles evaporating as they convect to regions of higher temperature. Note that the larger agglomerates in the figure may have been collected as the TEM grid was insert into the flame, unavoidably passing into the region of very large or very numerous particles, as shown in Figure 3.

For the counterflow flames, the appearance of the particles is similar. To extract the sample, the TEM grid was inserted perpendicular to the plane of the flame, at the centerline of the burner, into the center visible flame [43]. Figure 9 shows the electron micrograph of part of the sample grid which was inserted into a counterflow diffusion flame of methane and air with 300 µL/L or Fe(CO)$_5$ added to the air stream. In general, the degree of agglomeration is much smaller than that in the premixed flame. Primary particle sizes range from 5 nm to 25 nm in diameter.
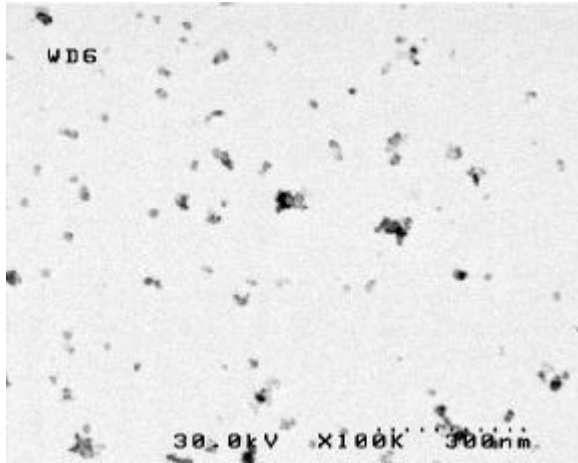
Figure 8 : Electron micrograph of particles sampled from a CH₄/air premixed flame with X_{inh} = 200 μL/L (from ref. [22]).
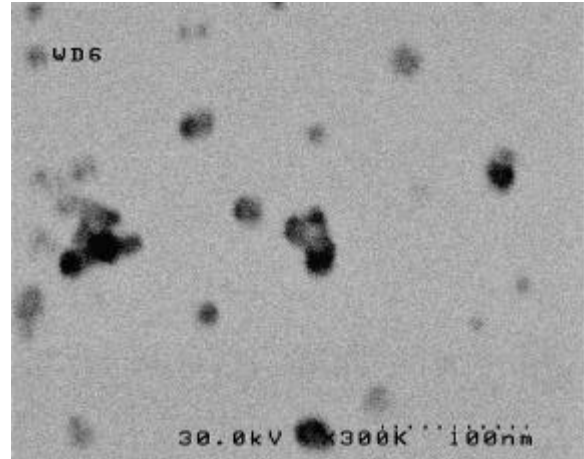
Figure 9 - Electron micrograph of particles sampled from counterflow dif-fusion flame at a = 150 s⁻¹ and X_{inh} = 300 μL/L (from ref.: [43]).

Estimate of Upper Limit of Heterogeneous Inhibition

Although the evidence presented above supports a gas-phase inhibition mechanism of $Fe(CO)_5$, it is possible that heterogeneous chemistry also makes a contribution. The effects of walls on radical chain branching with regard to explosion limits are well documented [44], and heterogeneous iron and iron oxide catalysts are widely used in industrial processes. Further, iron oxide particles have recently been proposed as catalysts for NO_x reduction in stationary combustors [45]. With some assumptions, we can estimate the upper limit of radical recombination by collisions with particles, and determine the maximum effect of the particles on the burning velocity. To provide this upper limit, we assume: 1.) a two-step heterogeneous inhibition mechanism (Langmuir-Rideal type) in which a radical is absorbed onto a particle surface $R+P \rightarrow RP$, followed by the reaction of the activated particle RP with another radical and the release of the stable species $RP+R \rightarrow R_2+R$; 2.) all of the iron present condenses to particles; 3.) the particles are spherical with a specified mean diameter d_m and log-normal size distribution; 4.) all collisions of radicals with particles lead to their recombination; 5.) only H-atom recombination is considered (the additional benefit of adding OH and O recombination is minor). The calculation is implemented using the PREMIX code and with the particles represented as fictitious species with the required rate parameters [22]. The results of the calculation are shown in Figure 10 for particles of diameter 10 nm to 80 nm. Also shown for comparison are experimental data (points) for $Fe(CO)_5$ inhibition of the premixed methane-air flames [9], and the results of a calculation for a proposed perfect gas-phase inhibitor [46] (bottom curve). In the perfect gas-phase mechanism, collisions of a chain-carrying radical with <u>any</u> gas-phase intermediate species of the inhibitor result in trapping of the radical. As the figure shows, the heterogeneous mechanism does show significant flame inhibition, which increases as the assumed particle diameter decreases. Nonetheless, the inhibition from the heterogeneous mechanism is not as strong as that shown by the experiment or by the perfect gas-phase inhibition mechanism.

13
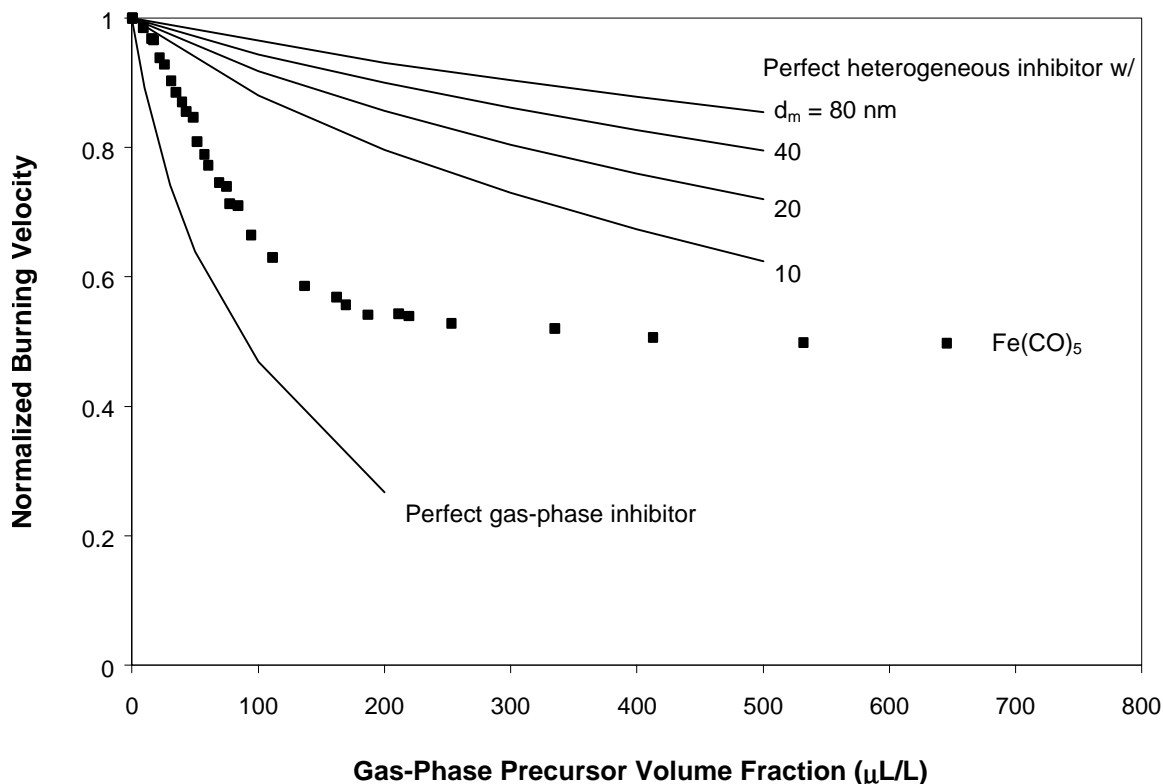
Figure 10: Calculated normalized burning velocity for several diameters d$_m$ of ideal heterogeneous inhibitor. Also shown are Fe(CO)$_5$ data [9], and calculated normalized burning velocity using the perfect gas-phase inhibitor mechanism [46] (from ref. [22]).

The results of the calculations presented in Figure 10 support the importance of a homogeneous inhibition mechanism of iron rather a heterogeneous one. The formation of particles essentially increases the number of inhibitor molecules per particle, and increases the particle mean diameter d$_m$. Since of the number of particles scales as $1/d_m^3$, but the collision cross section of particles with radical scales as $1/d_m^2$, the net effect of particle formation is to decrease the collision rate of radicals with inhibiting species. These idealized calculations support the proposals [9,46] that only gas-phase chemistry is fast enough to account for the extraordinary inhibition effect of Fe(CO)$_5$, since a more realistic model of heterogeneous radical recombination would probably result in less inhibition. It is interesting to note that the residual inhibition of Fe(CO)$_5$ at $X_{in} > 300$ µL/L in Figure 10, while small compared to values at $X_{in} < 100$ µL/L, is not zero. It is, in fact, comparable to agents such as CF$_3$Br and may be due to heterogeneous inhibition.

Counterflow Diffusion Flames

Laser scattering experiments to detect the presence of particles were also conducted in counterflow diffusion flames [43]. For these flames, the measurements were made along a vertical profile at the centerline of the fuel and oxidizer tubes. Figure 11 shows the scattering signal as a function of the distance from the center of the methane and air jets. The data points

14

(connected by lines) correspond to values of Fe(CO)$_5$ volume fraction of (0, 50, 100, and 300) µL/L. The calculated gas temperature [20] as a function of distance from the center of the jets is shown by the top scale, and the calculated gas-flow stagnation plane is indicated by the vertical line. As the figure illustrates, the particles form in the low-temperature region on the air side of the flame, at temperatures below 500 K. Interestingly, as in the premixed flames, the particles are nearly completely consumed by the time they reach the location of the peak flame temperature (1961 K), and then re-form as they approach the stagnation plane. For this flow field, however, the residence time gets much longer as the particles approach the stagnation plane, allowing much time for particle growth. Further, as discussed below, thermophoretic forces cause the particles to cross the stagnation plane and reach an area of particle stagnation, which corresponds roughly to the location of the peak particle scattering signal, and occurs on the fuel side of the gas stagnation plane.
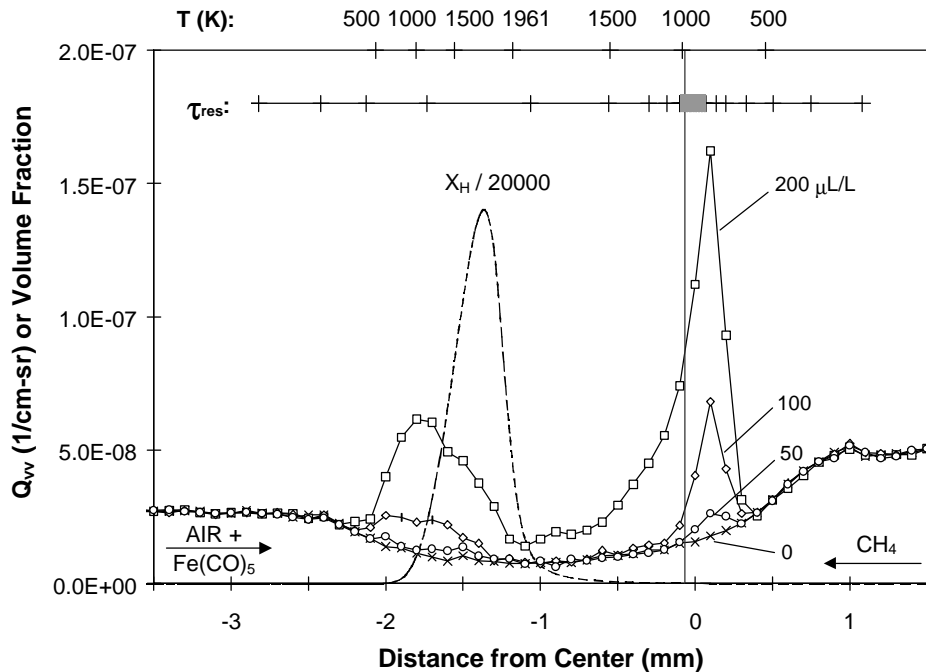
Figure 11 - Methane-air counterflow diffusion flame with inhibitor in the oxidizer. Shown are the calculated temperature (upper scale), stagnation plane location (vertical line), and H-atom volume fraction (dashed line) for the uninhibited flame, and the measured scattering profiles (connected points) for Fe(CO)$_5$ volume fractions of (0, 50, 100 and 200) µL/L in the air stream ($a = 330$ s^{-1} , which is 50 % of a_{ext} for the uninhibited flame and 77 % of a_{ext} for $X_{in} = 200$ µL/L). The estimated residence time for 5 nm particles is shown as 10 ms intervals in the hatched line near the top (from ref.: [43]).
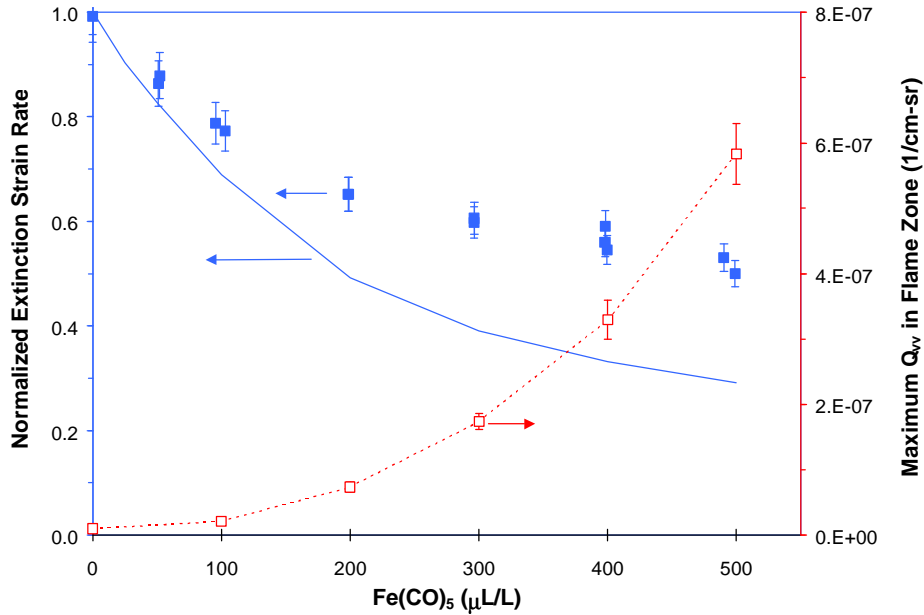
Figure 12: Correlation between inhibition effect and maximum Q_{vv} . Filled points are experimental normalized a_{ext} , solid line is calculated a_{ext} ([20]). Open symbols connected by dotted lines are maximum measured Q_{vv}. Particle data collected at 75 % of a_{ext} (from ref.: [43]).

Thermophoresis is important for the movement of small particles in these counterflow flames. Based on the gas-phase flame structure obtained from numerical calculations of uninhibited flames, we calculated the thermophoretic velocity of particles 5 nm in diameter [43]. Combining these with the gas-phase velocity, we determined the residence time of 5 nm particles injected from either the fuel or air jet. The hatched line near the top of Figure 11 shows the particle residence time (as 10 ms intervals between the hatch marks). Near the particle stagnation region, the near-zero particle velocities create large uncertainties in the estimated residence time (caused in part by the limited spatial resolution of the numerical flame structure calculation); this region is indicated by the shaded bar on the line showing the residence time. The inclusion of the thermophoretic velocity of the particles shows that 5 nm particles are expected to cross the stagnation plane about at the location of the fuel-side scattering peak, explaining its existence.

The formation of the particles on the *air* side of the gas stagnation plane is the likely cause of the loss of inhibition. With addition of $Fe(CO)_5$ to the air stream, the air-side scattering signal increases, even for values of X_{inh} as low as 50 µL/L. The dotted line in Figure 11 illustrates the calculated H-atom volume mole fraction in the uninhibited flame. The location of the peak particle scattering (about 1.75 mm) overlaps with the region of high H-atom mole fraction. Catalytic radical recombination cycles are most important in the regions where radical mole fractions are the highest (and iron species most strongly catalyze H-atom recombination). Hence, particles forming near the peak [H] can sequester the active gas-phase iron-containing intermediate species and thereby reduce the strength of the catalytic cycles.

The loss of effectiveness of $Fe(CO)_5$ in counterflow diffusion flames can be directly correlated with the formation of the air-side scattering peak from particles. Following the approach

described above for premixed flames with $Fe(CO)_5$, the presence of particles is quantified by the height of the air side scattering peak (minus the scattering signal from the gas-phase species). Figure 12 shows the normalized extinction strain rate (left axis) as a function of the $Fe(CO)_5$ volume fraction in the air stream. As in the premixed flames, the inhibitor is very effective at low values of X_{inh}, but loses its effectiveness sharply as X_{inh} reaches a certain value (about 150 µL/L for these conditions). Similarly, the normalized extinction strain rate calculated using a gas-phase only kinetic mechanism [19] (solid line in Figure 12) follows the experimental data reasonably closely for $X_{inh}<100$ µL/L, but starts to deviate as X_{inh} increases. The measured scattering cross section (right axis; open squares connected by dotted lines) shows that the scattering signal increases noticeably when the $Fe(CO)_5$ reaches the point of lower marginal effectiveness (~150 µL/L). As in the premixed flames, the *loss* of effectiveness of the $Fe(CO)_5$ is correlated with particle formation, rather than the converse.

Particle formation followed by flow-field effects can also *prevent* metallic inhibitors from entering into gas-phase catalytic radical scavenging reactions. To illustrate this, Figure 13 shows the scattering cross section from a counterflow methane-air diffusion flame with $Fe(CO)_5$ added to the *fuel* side of the stagnation plane at various values of X_{inh}. The calculated temperature field, residence time estimate, and location of peak [H] are the same as in Figure 12 for air-aide agent addition. In the case of fuel-side $Fe(CO)_5$ addition shown in Figure 13, the iron-containing species also start to condense at local gas temperatures less then 500 K. In this case, however, the thermophoretic forces *prevent* the iron from crossing the stagnation plane, and the scattering signal reaches its peak value near the calculated particle stagnation region for 5 nm particles. The scattering signal at the particle stagnation plane is two orders of magnitude larger for fuel-side agent addition than for air-side addition. Thus, fuel-side agent addition leads to particle formation, which together with thermophoretic and flow-field effects, effectively prevents the active species from reaching the location of peak [H]. For the methane-air flames of Figure 13, however, the $Fe(CO)_5$ added to the fuel stream would not be expected to inhibit the flame, even if the particles did not form. This is illustrated in Figure 14, which shows the reduction in the normalized extinction strain rate (left axis) with added $Fe(CO)_5$ to the fuel stream. For both the experimental data and the numerical predictions (based on a gas-phase only model), the inhibition of the flame is minimal. The increase in the scattering signal (right axis) with added $Fe(CO)_5$, however, is very large. As discussed previously [20], the $Fe(CO)_5$ added to the fuel stream is ineffective even if it remains in the gas phase; to be effective, the inhibiting species (or their precursors) must diffuse upstream into the oxidizer stream and reach the location of significant H-atom mole fraction. For these flames, however, the convective flow is larger than the diffusive flow, so the inhibitor (or its fragments) can't get to where it is required for radical recombination.
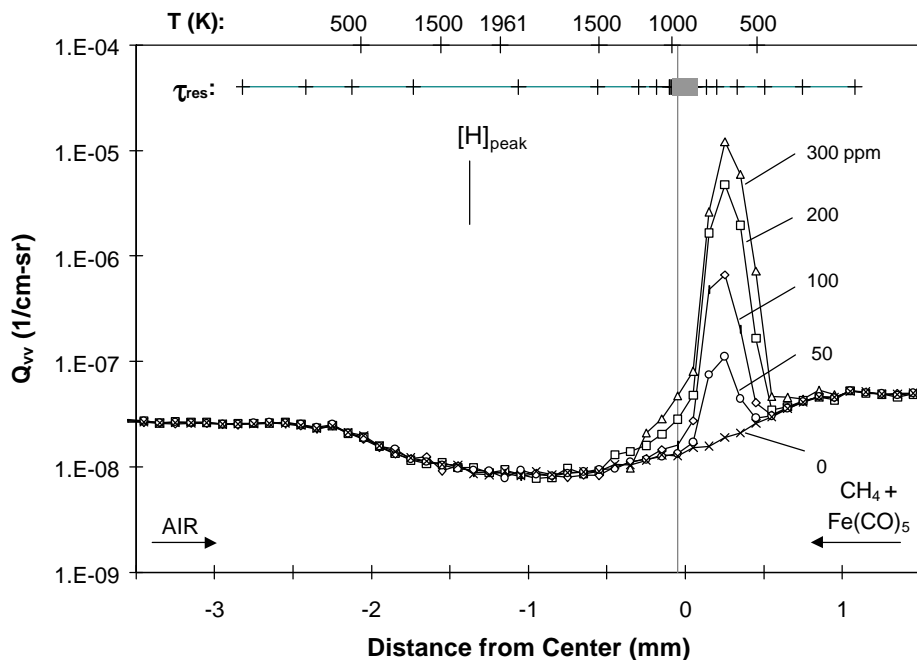
Figure 13: Measured scattering profiles in CH_4-air counterflow diffusion flame with inhibitor in the fuel. The calculated temperature and point of peak H-atom mole fraction are marked on the upper x-axis, and the vertical line denotes the calculated location of the stagnation plane. Strain rate = 330 s^{-1} (from ref.: [43]).
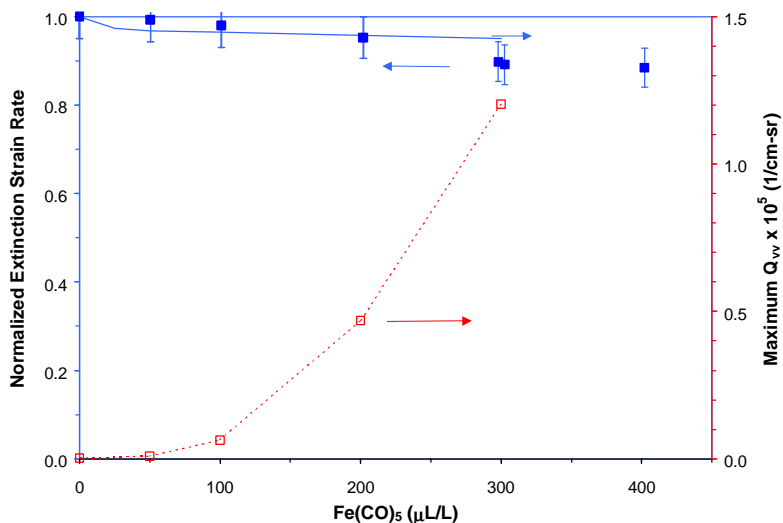
Figure 14 – Effect of $Fe(CO)_5$ added to the fuel stream of a methane-air counterflow diffusion flame. The experimentally measured and numerically calculated normalized extinction strain rate [20] are shown (left axis) as a function of $Fe(CO)_5$ volume fraction in the fuel stream. The maximum scattering cross section (right axis), obtained from the results in Figure 13 is also shown for increasing X_{inh}.

The importance of particle convection can be more clearly illustrated by considering a counterflow diffusion flame with the peak temperature and [H] closer to the stagnation plane, where gas-phase inhibiting species could diffuse. Such a flame is obtained from an oxidizer with volume fractions of 30 % O_2 / 70 % N_2 , and a fuel of 80 % CH_4 / 20 % N_2. The results of particle measurements for $Fe(CO)_5$ added to the air stream of such a flame is shown in Figure 15. For this flame, both the peak temperature and [H] are slightly on the fuel side of the gas stagnation plane (vertical line), while the particle stagnation plane (shaded box on the residence time bar at the top) is slightly on the oxidizer side. Clearly, very large particle scattering signals are present, and as in Figure 13 above, the particles do not appear to have significantly crossed the gas stagnation plane, and hence cannot deliver the active species to the region of high [H]. Unlike in Figure 13, however, the gas-phase inhibiting species *can* diffuse to the region of high [H]. This is illustrated in Figure 16, which shows the experimental measured and numerically calculated reduction in the normalized extinction strain and the particle scattering cross section for increasing amounts of $Fe(CO)_5$ in the air stream. Based on the experiments, adding $Fe(CO)_5$ has little effect on this flame. The calculations, however, which are based on a gas-phase model, predict that the added $Fe(CO)_5$ should have a significant effect (implying that the gas-phase species *can* diffuse to the location of the peak [H] (shown in Figure 15).   Nonetheless, the scattering measurements show prominent particle formation. Since, in Figure 15, both the gas stagnation plane (vertical line) and the particle stagnation region (shaded box on residence time bar at top) separate the particles from the region of peak [H], the particles can effectively isolate the active intermediate species from the location of H-atom where they are required to inhibit the flame. Consequently, we see in Figure 16 that while the gas-phase model (solid line) implies that inhibition should occur with addition of $Fe(CO)_5$, the experiments (points) do not show inhibition, and this is consistent with the large scattering signal (dotted line) observed with addition of the $Fe(CO)_5$.

The results presented for the counterflow diffusion flames with added $Fe(CO)_5$ illustrate the following *physical* phenomena which can influence the efficiency of the inhibitor. 1.) The rate of gas-phase transport of the active inhibiting species to the location of peak [H], either by diffusion or convection; 2.) Particle formation, which can reduce the availability of active gas-phase species either by: a.) reducing the gas-phase volume fraction of the active iron-containing intermediate species in the vicinity of the peak [H], or b). physically separating the particles from the region of peak [H] by flow field and thermophoretic effects. This background information is essential for understanding the relevant phenomena affecting the action of metallic inhibitors when added to the more complex flow field of the cup-burner flames, as described below.
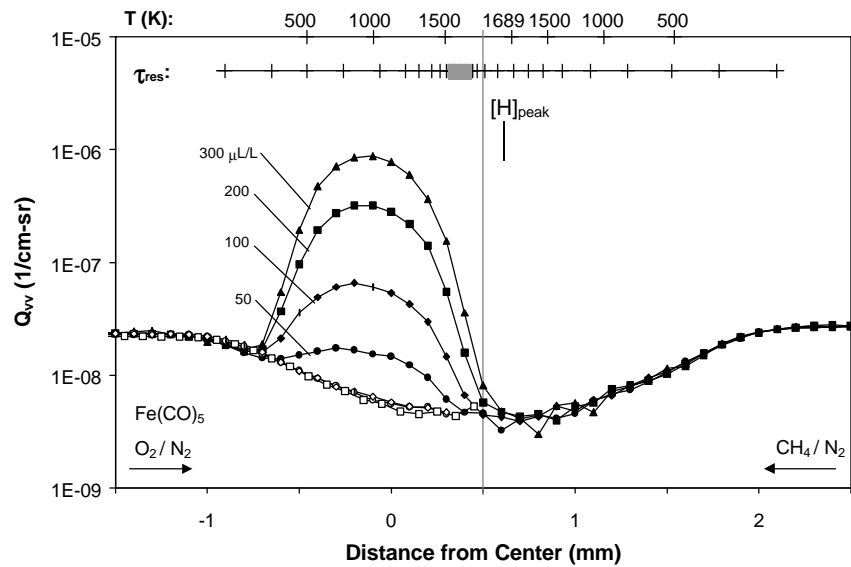
Figure 15 - Scattering profiles through a counterflow diffusion flame of 30 % O_2/70 % N_2 and 80 % CH_4/N_2. The calculated temperature and point of peak H-atom mole fraction are marked on the upper x-axis, and the vertical line denotes the calculated location of the stagnation plane. $Fe(CO)_5$ is added to the oxidizer stream at the indicate volume fraction. The estimated residence time for 5 nm particles is shown as 10 ms intervals in the hatched line near the top (from ref.: [43]).
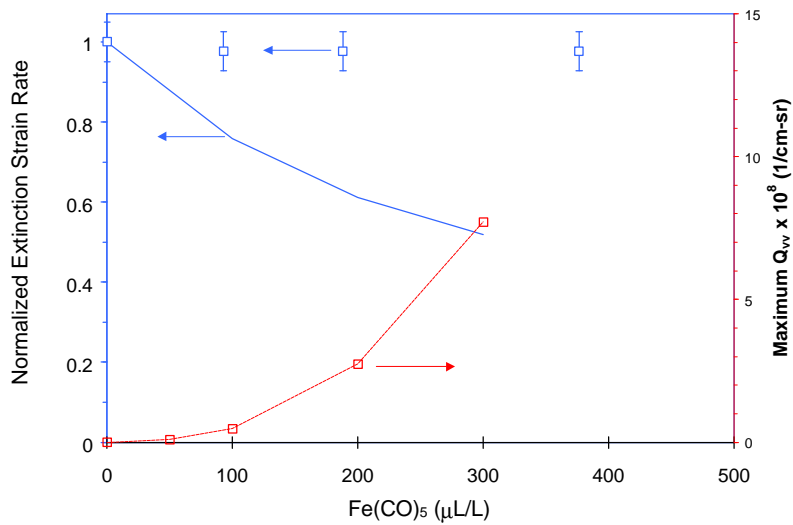
Figure 16 - Effect of $Fe(CO)_5$ added to the air stream of a diluted methane-air counterflow diffusion flame. The experimentally measured (points) and numerically calculated (solid line) normalized extinction strain rate [20] are shown (left axis) as a function of $Fe(CO)_5$ volume fraction in the air stream. The maximum scattering cross section (right axis), obtained from the results in Figure 13 is also shown for increasing X_{inh}.

Cup-Burner Flames

Cup-burner type co-flow diffusion flames were also tested with Fe(CO)$_5$ added as a flame inhibitors. As described above, based on the premixed and counterflow diffusion flame results, it was suspected that Fe(CO)$_5$ alone would not be effective at extinguishing cup burner flames. This is because addition above some limiting volume fraction would just lead to more and more condensation, while not increasing the gas-phase concentration of the inhibiting species. Flame extinguishment would eventually occur from some far less efficient processes, for example, oxygen starvation or thermal effects from the added compound. Nonetheless, it was expected that addition of Fe(CO)$_5$ together with an inert compound should reduce the amount of inert required for flame extinguishment (especially if the volume fraction of Fe(CO)$_5$ is kept below its saturation vapor pressure) [10]. In the present experiments, CO$_2$ was added as the fire suppressant to extinguish the methane-air cup burner flames. The organometallic compound was added to the air stream at a fixed volume fraction, and the volume fraction of CO$_2$ in the oxidizer stream required to extinguish (i.e., blow off) the flame (X$_{CO_2,ext}$) was determined. The tests were conducted for a range of metallic inhibitor volume fractions in air, using the agents Fe(CO)$_5$, MMT, or TMT, as well as for Br$_2$ and CF$_3$Br.

For inhibiting cup-burner flames, the organometallic agents TMT, MMT, and Fe(CO)$_5$ were found to be far less efficient than they were in either premixed or diffusion flames. Figure 17 shows the volume fraction of CO$_2$ in the oxidizer stream required to blow off a cup-burner flame (X$_{CO_2,ext}$) as a function of the volume fraction of added catalytic inhibitor in the air part of the oxidizer stream [15]. Data are presented for CF$_3$Br, Br$_2$, TMT, Fe(CO)$_5$, and MMT, as well as for a blend of TMT, MMT, and Fe(CO)$_5$. The inset of Figure 17 shows the region of interest (low inhibitor volume fraction) with expanded scales. The agents CF$_3$Br and Br$_2$ are shown to effectively reduce the amount of CO$_2$ required to extinguish the flame. The metallic agents reduce the amount of required CO$_2$ somewhat more effectively than does CF$_3$Br, but they lose their effectiveness in a manner that is similar to that described above for premixed and diffusion flames. In the cup-burner flames, TMT, MMT, and Fe(CO)$_5$ were approximately 3, 8, and 4 times as effective as CF$_3$Br, in contrast to premixed flames, in which they were 3, 40, and 80 times as effective. The net result is that the metallic agents were not particularly effective in cup-burner flames. This result was surprising, and further work was conducted to understand the loss of effectiveness.

21
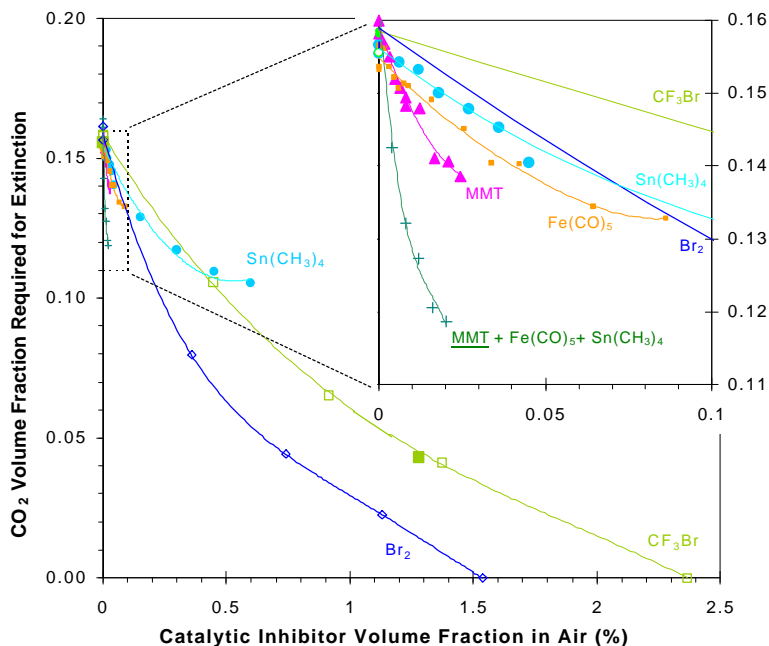
Figure 17 – Volume fraction of CO$_2$ required for extinction ($X_{CO_2,ext}$) of methane-air cup burner flames as a function of the volume fraction of catalytic inhibitor added to the air stream. Inset shows region in dotted box with expanded scales.

Particle formation is likely the cause of the degraded performance of the metal agents in cup-burner flames. Evidence to support this is that the approximate agent volume fraction for the loss of effectiveness is an order of magnitude higher for TMT (4000 µL/L) than for the iron or manganese (400 µL/L) (as occurs in premixed flames) [11], which is consistent with the higher vapor pressure for the tin compounds. Also, the manner in which Fe-, Sn- and Mn-containing compounds lose their effectiveness in premixed flames [11] is comparable to that indicated in Figure 17 (inset). Finally a visible outer annulus, apparently particles, was observed in all flames with added metals, and the blackbody radiation from that region increased with higher agent volume fraction.

To more accurately detect the particles, we conducted laser-scattering experiments in the cup-burner flames with and without added Fe(CO)$_5$. The scattering measurements were made on several horizontal paths across the flame at fixed heights above the fuel-cup rim. Although methane-air cup burner flames are unsteady, flickering at about 10 Hz with a large amplitude, steady, nearly non-flickering flames are achieved with addition of CO$_2$ to the air stream. Hence, scattering measurements in cup-burner flames with Fe(CO)$_5$ added to the air stream were performed with a CO$_2$ volume fraction of 8 % in the air stream. This approach was reasonable since the extinction tests were also conducted with appreciable volume fractions of CO$_2$. The agent Fe(CO)$_5$ was added to the air stream at (0, 100, 200, 325, and 450) µL/L. Figure 18 to Figure 21 present radial profiles of the scattering cross section (arbitrary but consistent units) at heights above the burner rim of (3, 6, 10, 15, and 20) mm. Also shown in each figure is the location of the peak visible emission, obtained from a digitized video image of the flame with 0

22

μL/L of $Fe(CO)_5$. Since the oxygen demand of the $Fe(CO)_5$ in the oxidizer stream at 450 μL/L is about 0.6 % that of the methane, the flame location should not be significantly modified by presence of this fuel-like agent in the co-flow [47]. In Figure 18 to Figure 21, the peak scattering signal detected is (1.1, 4.7, 12.7, and 25.5) x 10^{-6} 1/(cm-sr), respectively, which are 50, 209, 559, and 166 times the scattering signal for air at laboratory conditions. In all cases, the presence of particles is clearly indicated, and the magnitude of the scattering signal increases with $Fe(CO)_5$ volume fraction in the air. For each value of X_{inh} , the relative distribution of the particles for each height and radial position is approximately conserved. Particles are present both inside and outside, but not coincident with, the visible flame location. Flames without $Fe(CO)_5$ (not shown) had scattering cross sections attributable to only the hot and cold product and reactant gases.

In order to interpret the scattering results shown in Figure 3, it is useful to consider the particle measurements in the premixed [22] and counterflow diffusion flames [43] seeded with $Fe(CO)_5$. From the above results, it appears that: 1.) the iron-containing species start to condense as the temperature increases to about 500 K , which is hot enough to breakdown the iron precursor [19], but not too hot to vaporize the iron compound; 2.) the particles are small, ~10 nm to 20 nm; 3.) thermophoresis moves the particles away from the peak temperature; 4.) drag forces tend to entrain the particles along the gas flow streamlines; 5). particles can re-vaporize as they enter regions of high temperature; 6.) longer residence times lead to a greater scattering signal (and presumably, a greater fraction of condensed species); and 7.) more $Fe(CO)_5$ leads to a larger scattering signal. In order for the iron species to have a chemical effect on the flame, they must: 1.) reach the region of peak [H] as gas-phase species; 2.) be active in a region which affects the flame stability (and hence, the blow-off condition).
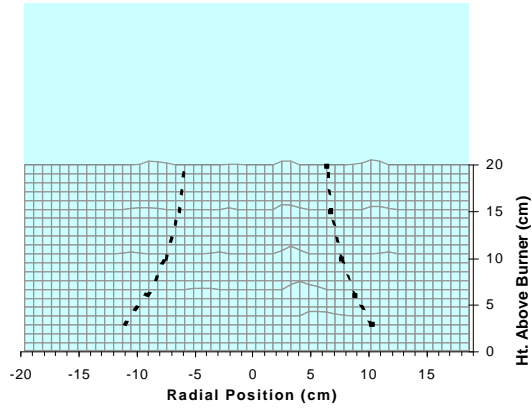
Figure 18 to Figure 21 – Scattering cross section for laser light at 488 nm as a function of radial position and height above burner in methane-air cup-burner flame with 8 % CO_2 and $Fe(CO)_5$ in air at specified volume fraction . Dotted lines show flame location from a digitized video image of the uninhibited flame.

Figure 18 - $Fe(CO)_5$ in air at 100 μL/L.
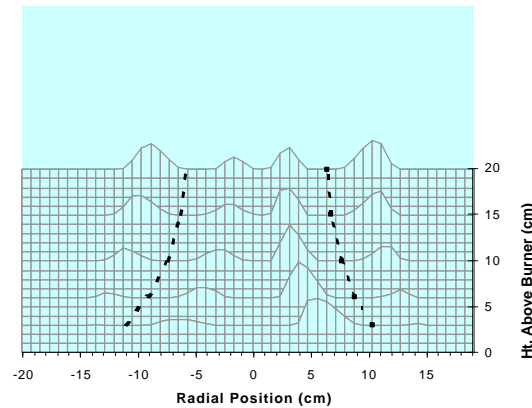
Figure 19 – $Fe(CO)_5$ in air at 200 μL/L.
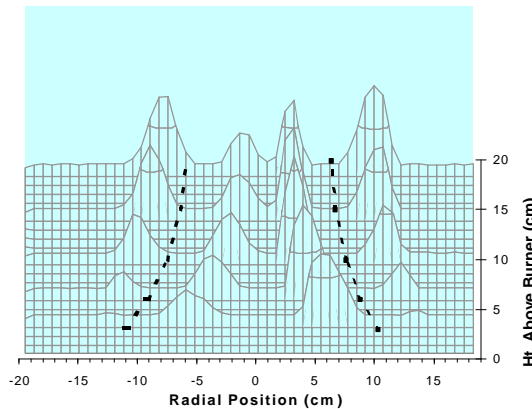
Figure 20 – $Fe(CO)_5$ in air at 325 μL/L.
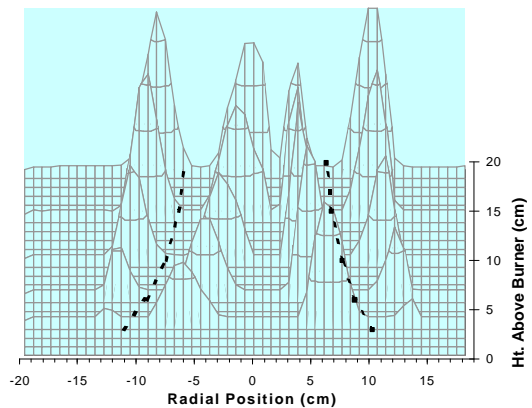
Figure 21 – $Fe(CO)_5$ in air at 450 μL/L.

Since the present cup-burner flames have quite different flow fields than either premixed or counterflow diffusion flames, it is likely that the particle formation and behavior in them is different. For example, iron added to the air stream of either the premixed or counterflow diffusion flame eventually must pass through the flame by convection. In contrast, convection is comparatively less important in co-flow diffusion flames. Further, thermophoretic forces can have a strong influence on particle trajectories in flames [48]. Recent attempts to seed co-flow diffusion flames with $TiCl_4$ to provide very small TiO_2 for laser imaging of the velocity field proved ineffective due to strong thermophoresis of the particles [49]. For the present co-flow diffusion flames, the thermophoretic forces are nearly tangent to the flow streamlines, so their relative importance will be greater. Also, as discussed by Faeth et al. [50], the flow streamlines tend to enter the flame near the burner jet exit, and then remain approximately parallel to the temperature contours before again crossing the flame near the tip. Hence, iron could enter the center region from convection into the flame near the base (providing the iron inside the flame sheet for particle formation). Thermophoresis could then push the particles away from the flame sheet, resulting in the particle distribution shown in Figure 18 to Figure 21. Alternatively, the particles may still be present in the region of peak [H], but may be too small to be detected at the lock-in sensitivity used to resolve the larger scattering signals.

It is possible to plot the flame inhibition strength as a function of added $Fe(CO)_5$ for comparison with the particle scattering signal. Figure 22 shows such a plot, which can be compared to Figure 5, Figure 12, and Figure 16 for premixed and counterflow diffusion flames (with pure and diluted gases). The added iron has little effect on the amount of CO_2 required for extinction, yet the peak particle scattering signal clearly increases with added iron. What is missing from Figure 22 is a model prediction to show that for gas-phase inhibiting species, a reduction in CO_2 for flame extinction is expected. While such calculations are desired (but as yet unavailable for the cup burner), we can still infer the active role of gas-phase species from the data available. For example, both CF_3Br and Br_2 added to the air stream were very effective at reducing the CO_2 for extinction. Hence, catalytically acting gas-phase agents which don't condense do reduce the amount of CO_2 required for extinction.

Methane-Air Cup Burner
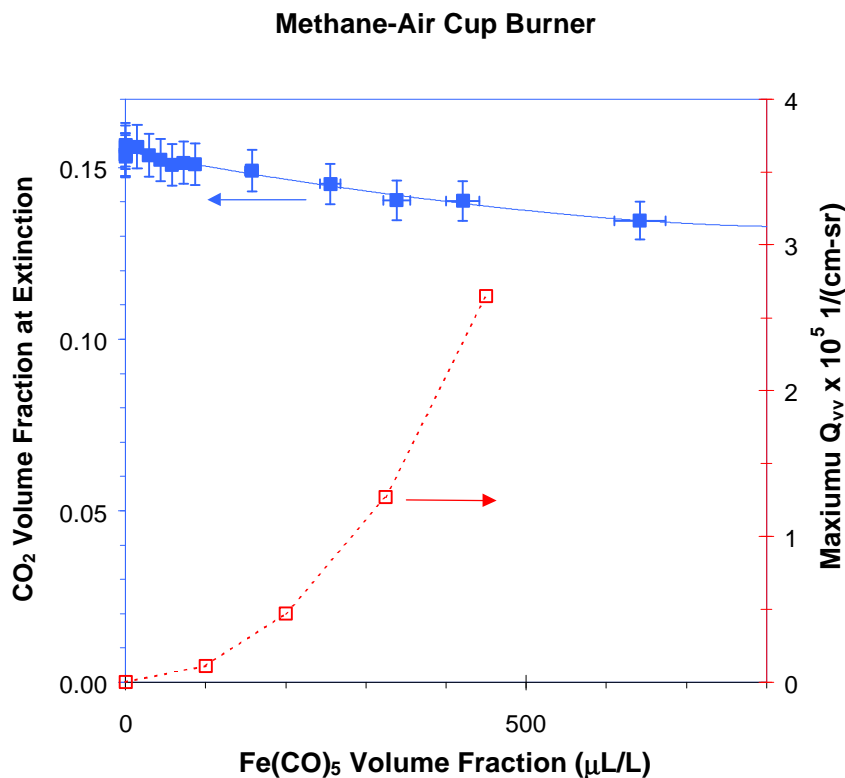
Figure 22 – Extinction volume fraction of CO_2 (left axis) [15] and peak measured scattering cross section (right axis), as a function of the volume fraction of $Fe(CO)_5$ in the air stream.

From the ineffectiveness of iron when added to the cup burner (as shown in Figure 17), it seems that the iron species of the catalytic cycle are not reaching the regions of the flame in which they are need to cause flame destabilization and blow-off. Examination of Figure 18 to Figure 21 shows that the iron particles are not coincident with the visible flame location. One might infer that this means that 1.) the iron is sequestered in the particles, and 2.) the particles are kept away from the high-temperature regions near the peak [H] by thermophoresis, and 3.) these lead to a low value of the gas-phase volume fraction of the iron-containing intermediate species near the peak [H]. While these features are probably true in the flame, it is not possible to extract this understanding from the data available.

At the present time, the location of the stabilization region of the cup burner flame most sensitive to chemical inhibition is not known, nor are the H-atom concentration profiles or the flow streamlines. These data would provide a much clearer explanation of the effects of particles on iron inhibition of cup-burner flames.

Conclusions

The organometallic agents TMT, MMT, and $Fe(CO)_5$, which were found previously to be effective in premixed flames, were virtually ineffective in cup-burner type co-flow diffusion

26

flames. While these agents do reduce the amount of CO_2 required to extinguish the cup-burner flames when added at low volume fraction (less than a few hundred μL/L), they quickly lose their marginal effectiveness, so that their total effect is small. Further, their efficiency even at the low volume fractions is far less than in premixed or diffusion flames. Since particle formation has been found to be important in other flame types inhibited by organometallic agents, laser scattering measurements were conducted in cup-burner flames with $Fe(CO)_5$ added to the air stream. Large scattering signals indicated that particles are present both inside and outside of the flame, but not co-incident with the visible flame location.

A review of the results from previous work with particle formation in premixed and counterflow diffusion flames inhibited by $Fe(CO)_5$ outlined the importance of the following physical effects with respect to effective chemical inhibition:

1.) gas-phase transport of the active iron-containing species to the region of high H-atom concentration is necessary for efficient inhibition.
2.) Particle formation near the location of peak [H] can act as a sink for the iron-containing intermediate species and reduce the catalytic effect.
3.) The volume fraction of inhibitor influences condensation since at low values, it may be below its saturation value.
4.) The available residence time affects particle growth.
5.) Thermophoretic forces can be large in the flame and re-distribute particles away from peak [H].
6.) Convection and drag forces combined with the existing flow field in the flame can prevent particles from reaching the region of peak [H].

Using this information we can infer that particles start to form in the cup-burner flames in regions where $Fe(CO)_5$ is transported and when the temperature has risen slightly (to allow decomposition of the precursor molecule $Fe(CO)_5$). These particles act as sinks for the active species, reducing their overall catalytic ability. Thermophoretic forces (which are tangent to the flow streamlines) move the particles away from the region of peak temperature and [H].

Nonetheless, the actual regions in a cup-burner flame which are most sensitive to chemical inhibition are not known for *any* catalytic agent. The work illuminates the need for detailed measurements and numerical modeling (with full chemistry) of cup-burner flames so that the actions of chemical inhibitors in such flames can be more clearly discerned.

Acknowledgements

References

[1] Andersen, S.O., *Fire Journal* 81:56-& (1987).

[2] Grosshandler, W. L., Gann, R. G., and Pitts, W. M., *Evaluation of Alternative In-Flight*

Fire Suppressants for Full-Scale Testing in Simulated Aircraft Engine Nacelles and Dry Bays, NIST SP 861, 1994.

[3]   Gann, R. G., *Fire Suppression System Performance of Alternative Agents in Aircraft Engines and Dry Bay Laboratory Simulations,* NIST SP 890, vols. I and II, 1995.

[4]   Miziolek, A. W. and Tsang, W., *Halon Replacements*, Acs Symposium Series 611, American Chemical Society, Washington, D.C., 1995.

[5]   MacDonald, M.A., Jayaweera, T.M., Fisher, E.M., and Gouldin, F.C., *Proceedings of the Combustion Institute, Vol. 27*, The Combustion Institute, Pittsburgh, 1998, pp.

[6]   Babushok, V. and Tsang, W., *International Conference on Fire Research and Engineering, Third*, Society of Fire Protection Engineers, Boston, MA, 1999, pp. 257-267.

[7]   Macdonald, M.A., Jayaweera, T.M., Fisher, E.M., and Gouldin, F.C., *Combust. Flame* 116:166 (1999).

[8]   Macdonald, M.A., Gouldin, F.C., and Fisher, E.M., *Combust. Flame* 124:668 (2001).

[9]   Reinelt, D. and Linteris, G.T., *Proc. Combust. Inst.* 26:1421 (1996).

[10] Linteris, G.T., Rumminger, M.D., Babushok, V., and Tsang, W., *Proc. Combust. Inst.* 28:2965 (2000).

[11] Linteris, G.T., Knyazev, K., and Babushok, V., *Combust. Flame* accepted (2001).

[12] Fallis, S., Holland, G.F., McCormick, J.L., Reed, R., and Wilson, K.A., *Halon Options Technical Working Conference*, Albuquerque, NM, 2001, pp. pp. 364-372.

[13] Lask, G. and Wagner, H.G., *Proc. Combust. Inst.* 8:432 (1962).

[14] Korobeinichev, O., Mamaev, A., Sokolov, V., Bolshova, T., Shvartsberg, V., Zakharov, L., and Kudravtsev, I., *Halon Options Technical Working Conference*, Albuquerque, NM, 2000, pp. 164-172.

[15] Linteris, G.T., *Proc. Combust. Inst.* 29:submitted (2002).

[16] Bulewicz, E.M. and Padley, P.J., *Proc. Combust. Inst.* 13:73 (1971).

[17] Bonne, U., Jost, W., and Wagner, H.G., *Fire Res. Abstracts Rev.* 4:6 (1962).

[18] Jost, W., Bonne, U., and Wagner, H.G., *Chem. Eng. News* 39:76 (1961).

[19] Rumminger, M.D., Reinelt, D., Babushok, V., and Linteris, G.T., *Combust. Flame* 116:207 (1999).

[20] Rumminger, M.D. and Linteris, G.T., *Fire Safety Science: Proc. of the Sixth Int. Symp.*,

Int. Assoc. for Fire Safety Science, Marne-La-Vallee, France, 2000, pp. 289-300.

[21] Rumminger, M.D. and Linteris, G.T., *Combust. Flame* 120:451 (2000).

[22] Rumminger, M.D. and Linteris, G.T., *Combust. Flame* 123:82 (2000).

[23] Linteris, G.T. and Truett, L., *Combust. Flame* 105:15 (1996).

[24] Andrews, G.E. and Bradley, D., *Combust. Flame* 18:133 (1972).

[25] Mache, H. and Hebra, A., *Sitzungsber. Österreich. Akad. Wiss.* IIa, 150:157 (1941).

[26] Puri, I.K. and Seshadri, K., *Combust. Flame* 65:137 (1986).

[27] Seshadri, K. and Williams, F.A., *Int. J. Heat Mass Transfer* 21:137 (1978).

[28] Hirst, B. and Booth, K., *Fire Technol.* 13:296 (1977).

[29] Linteris, G.T. and Gmurczyk, GW., in *Fire Suppression System Performance of Alternative Agents in Aircraft Engine and Dry Bay Laboratory Simulations* (R.G. Gann, Ed.), National Institute of Standards and Technology, Gaithersburg, MD, 1995.

[30] Gilbert, A.G. and Sulzmann, K.G.P., *J. Electrochem. Soc.* 121:832 (1974).

[31] Stull, D.R., *Ind. Eng. Chem.* 39:517 (1947).

[32] Hollrah, D., "Ethyl Corp., Personal Communication, Jan. 2001.

[33] Santoro, R.J., Semerjian, H.G., and Dobbins, R.A., *Combust. Flame* 51:203 (1983).

[34] Charalampopoulos, T.T., Hahn, D.W., and Chang, H., *Appl. Opt.* 31:6519 (1992).

[35] Dibble, R. W., Ph.D. Dissertation, University of Wisconsin, Madison, 1975.

[36] Nguyen, Q.-V., Ph.D. Dissertation, University of California, Berkeley, 1995.

[37] Rudder, R.R. and Bach, D.R., *J. Opt. Soc. Am.* 58:1260 (1968).

[38] D'Alessio, A., in *Particulate Carbon: Formation during Combustion* (Siegla, D. C. and Smith, G. W., Ed.), Plenum Press, New York, pp. 207-256, 1981.

[39] Dobbins, R.A. and Megaridis, C.M., *Langmuir* 3:254 (1987).

[40] Koylu, U.O., Mcenally, C.S., Rosner, D.E., and Pfefferle, L.D., *Combust. Flame* 110:494 (1997).

[41] Taylor, B. N. and Kuyatt, C. E., *Guidelines for Evaluating and Expressing the Uncertainty of NIST Measurement Results,* National Institute of Standards and Technology, NIST Technical Note 1297, 1994.

[42]   Rumminger, M.D. and Linteris, G.T., *Proc. Combust. Inst.* 29:submitted (2002).

[43]   Rumminger, M.D. and Linteris, G.T., *Combust. Flame* 128:145 (2002).

[44]   Glassman, I., *Combustion*, Acedemic Press, New York, NY, 1977.

[45]   Lissianski, V.V., Maly, P.M., Zamansky, V.M., and Gardiner, W.C., *Industrial & Engineering Chemistry Research* 40:3287 (2001).

[46]   Babushok, V., Tsang, W., Linteris, G.T., and Reinelt, D., *Combust. Flame* 115:551 (1998).

[47]   Roper, F.G., *Combust. Flame* 29:219 (1977).

[48]   Gomez, A. and Rosner, D.E., *Combust. Sci. Technol.* 89:335 (1993).

[49]   Takahashi, F., "NASA-Glenn, Personal Communication, Sept. 2001.

[50]   Urban, D.L., Yuan, Z.G., Sunderland, P.B., Linteris, G.T., Voss, J.E., Lin, K.C., Dai, Z., Sun, K., and Faeth, G.M., *AIAA J.* 36:1346 (1998).

Figure sources:

Figure	Sheet	File:
Figure 1	All Metals Norm wss	Manganese.xls
Figure 2	Internal Word Drawing in	Premixed Particle, final version.doc
Figure 3	Data of 032999 CH4-air	low and high
Figure 4	Data of 032999 CH4-air	Qvv
Figure 5	Data of 032999 CH4-air	Max Sca Chart
Figure 6	Data of 033199 CO-H2	Max Sca XH2 wss
Figure 7	Qvv vs. SL	Data of 032999 CH4-air
Figure 8	n/a	5-11-99neg.006
Figure 9	n/a	tem image of cf particles.jpg
Figure 10	NBV vs. Xin wss	Perfect Heterogeneous Inhibitor
Figure 11	Qvv	Data of 022399 FO-IO scatter
Figure 12	FO-IO wss	Data of 022499 FO-IO 75% scatter.xls
Figure 13	Qvv	Data of 022299 FO-IF Scatter.xls
Figure 14	FO-IF wss	Data of 022299 FO-IF Scatter.xls
Figure 15	Qvv a=368 IO wss	Data of 020199 FFd-IO, IF, 75% Scatter
Figure 16	FF-IO plot wss	Data of 020199 FF-IO, IF, 75% scatter.xls
Figure 17	wss inset	CUPBURNER.xls
Figure 18		Data of 112001 8% CO2, 100 ppm feco5.xls
Figure 19		Data of 112001 8% CO2, 200 ppm feco5.xls
Figure 20		Data of 112001 8% CO2, 325 ppm feco5.xls
Figure 21		Data of 112001 8% CO2, 450 ppm feco5.xls
Figure 22	wss scat vs feco5 uLL	CUPBURNER.xls

To do:

Check fig 1 source.
Near fig 17.